NJC

ROYAL SOCIETY OF CHEMISTRY

PAPER

View Article Online
View Journal | View Issue

Cite this: *New J. Chem.*, 2025, 49, 9166

An N-oxide-BODIPY-based ratiometric NIR fluorescent probe for the selective and sensitive detection of ferrous ions in real samples†

Arindam Mondal,[a] Sudip Mondal,[b] Adinath Majee [b] and Subrata Dutta *[a]

Received 29th January 2025,
Accepted 29th April 2025

DOI: 10.1039/d5nj00396b

rsc.li/njc

Iron plays a crucial role in biological processes such as oxygen transport and maintaining cellular redox balance. However, an imbalance in its labile ferrous form (Fe^{2+}) can cause oxidative stress and lead to various diseases. Detecting Fe^{2+} in complex environments requires advanced probes with high sensitivity, selectivity, and real-time monitoring capabilities. To address these challenges, we developed BDNO, a BODIPY-based N-oxide fluorescent probe that utilizes an N-oxide reduction mechanism for Fe^{2+} detection. BDNO exhibits dual fluorescence behavior in the presence of Fe^{2+} ions: a turn-on near-infrared (NIR) emission at 715 nm (λ_{ex} = 610 nm) with a large Stokes shift of 105 nm and a turn-off emission at 570 nm (λ_{ex} = 540 nm). The probe demonstrated excellent selectivity and sensitivity toward Fe^{2+}, with a detection limit of 41 nM and a rapid response time of less than 5 seconds. Additionally, BDNO allowed for simple, visual detection of Fe^{2+} using paper strips and cotton buds and successfully detected Fe^{2+} in various real samples, including apple juice, orange juice, wine, tap water, river water, and seawater. The probe's fast response, high selectivity, and reliable sensing capabilities make it a promising tool for applications in food safety, environmental monitoring, and biomedical research.

1. Introduction

Iron, an essential transition metal, is critical for many important biological processes, including oxygen transport, energy production, and cellular redox balance.[1–3] Iron mainly exists in two oxidation states in biological systems: ferrous (Fe^{2+}) and ferric (Fe^{3+}). The equilibrium between Fe^{2+} and Fe^{3+} depends on oxygen levels in the environment. Although Fe^{2+} is generally unstable, it can remain stable in oxygen-free conditions, particularly in the presence of reducing agents. Iron is often in the Fe^{2+} state inside cells because it is loosely bound to proteins and because of the high concentration of reducing agents such as glutathione.[4–6] Iron ions are vital for maintaining optimal health when present in adequate amounts but in excess, they cause oxidative damage to cells because of their ability to produce harmful ROS (reactive oxygen species) from molecular oxygen, which is linked to various diseases, including cancer, neurodegenerative disorders, and organ dysfunction.[7–13] Developing advanced tools for detecting iron, especially free Fe^{2+}, is crucial to better understand how iron influences health and disease.

Various spectroscopic techniques, including absorption spectroscopy,[14] spectrophotometry,[15,16] electrochemical methods,[17,18] colorimetry,[19,20] and fluorescence-based approaches,[21,22] have been explored for detecting Fe^{2+}. Among these, fluorescence-based techniques are particularly advantageous due to their simplicity and reliability. Commercially available fluorescent probes such as Calcein and PhenGreen have been widely used for Fe^{2+} detection.[23,24] However, these probes rely on fluorescence quenching (turn-off response) *via* chelation, often producing low Fe^{2+} selectivity.[25–28] Several turn-on fluorescent probes have been developed for Fe^{2+} detection, including systems based on Schiff bases, N-oxide chemistry, rhodamine, and coumarin derivatives.[24,29–51] Among these, N-oxide-based probes stand out due to their superior selectivity for Fe^{2+}. For example, RhoNox-1, reported by Nagasawa *et al.*, was the first turn-on fluorescent probe based on the N-oxide group for Fe^{2+} detection.[31] It utilizes the N-oxide group as a fluorogenic switch and was successfully applied to detect labile Fe^{2+} in live cells. The same group later on developed a library of N-oxide-based probes, including CoNox-1, FluNox-1, and SiRhoNox-1, for multi-wavelength detection of Fe^{2+} in live cells.[52] Additionally, Feng *et al.* developed an N-oxide-based NIR fluorescent probe, NRF-Fe^{2+}, which utilizes the fluorescence resonance energy transfer (FRET) mechanism to detect Fe^{2+} ions in cells.[53] This probe effectively monitors Fe^{2+} level fluctuations in ferroptosis and drug-induced liver injury. Recently, Kanvah *et al.* and Chattopadhyay *et al.*

[a] *Department of Chemistry, Sardar Vallabhbhai National Institute of Technology, Surat-395007, Gujarat, India. E-mail: subrata.d@chem.svnit.ac.in*
[b] *Department of Chemistry, Visva-Bharati (A Central University), Santiniketan 731235, India*

† Electronic supplementary information (ESI) available. See DOI: https://doi.org/10.1039/d5nj00396b

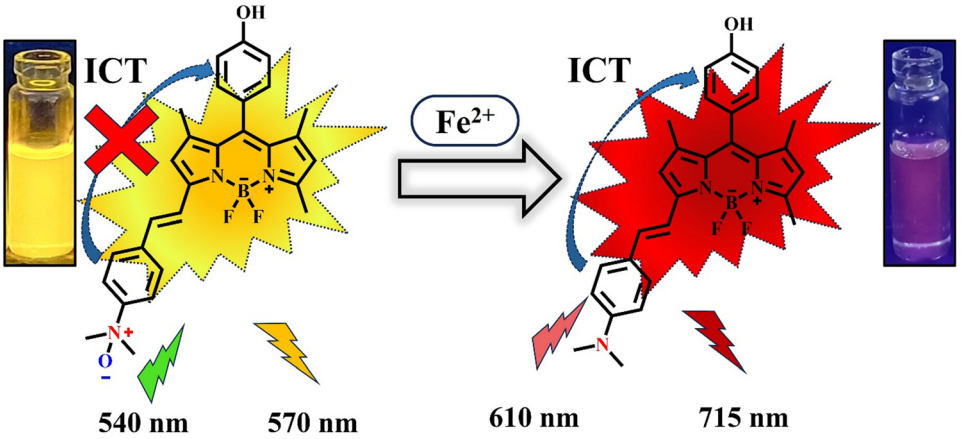

Scheme 1 Schematic representation of Fe^{2+} detection by BDNO through a ratiometric fluorescence response.

independently reported turn-on N-oxide-based probes for the detection of Fe^{2+} at nanomolar concentrations.[54,55] Despite considerable advancements, many fluorescent probes emit at shorter wavelengths, making them prone to interference from biological autofluorescence. Additionally, these probes often suffer from slow response times and high detection limits (LoD). Furthermore, most reported probes work as turn-on fluorescence sensors, but their signal can be easily affected by factors like instrument settings, environmental conditions, and probe concentration, leading to possible false-positive results. Therefore, ratiometric NIR fluorescent probes independent of the environmental effects are more desirable. In this work, we aimed to develop a fast, highly selective, and sensitive N-oxide-based ratiometric near-infrared (NIR) fluorescent probe for detecting Fe^{2+} to overcome the mentioned challenges. We designed and synthesized a ratiometric NIR fluorescent probe, BDNO, using an N-oxide-modified BODIPY. BDNO shows yellow fluorescence at 570 nm (λ_{ex} = 540 nm), which shifts to strong NIR fluorescence at 715 nm (λ_{ex} = 610 nm) when it reacts with Fe^{2+}, along with a decrease in the yellow emission. The probe initially displayed yellow fluorescence due to the suppression of intramolecular charge transfer (ICT). However, upon reduction of the N-oxide group to a dimethylamine moiety, the ICT mechanism was activated, stabilizing the excited state and shifting the fluorescence emission to the near-infrared (NIR) region (Scheme 1). This ratiometric response allows precise detection of Fe^{2+}. The probe detects Fe^{2+} within 5 seconds and has an exceptionally low detection limit of 41 nM, offering superior performance compared to several other reported probes (see Table S1 in ESI†). Additionally, BDNO demonstrated excellent performance in real samples, including apple juice, orange juice, red wine, and mineral water, highlighting its potential for practical applications for Fe^{2+} detection.

2. Experimental section

2.1. Materials and methods

Reagents and solvents used in this study were obtained from reliable commercial sources and were of analytical grade, ensuring the quality and reproducibility of the experiments. Specifically, 2,4-dimethyl-1*H*-pyrrole, 4-hydroxybenzaldehyde, and 4-(dimethylamino)benzaldehyde were procured from BLD pharm. Pyrrolidine and *meta*-chloroperoxybenzoic acid were purchased from Avra Synthesis. The progress of all reactions was closely monitored using TLC of Merck 60 GF254 silica gel plates. All chemicals and reagents were used without any purification.

2.2. Characterisation

^1H and ^{13}C NMR spectra were recorded on a Varian NMR spectrometer using DMSO-d_6 and CD_3OD as solvents. Mass spectra were measured with a Waters SQD2 mass spectrometer. UV-Vis studies were carried out using an IGene spectrophotometer, and fluorescence measurements were performed on an Agilent Cary Eclipse fluorescence spectrophotometer.

2.3. Synthesis procedure of BDNO

The compound BD (Scheme 2) was synthesized using the reported procedure.[56]

2.4. Synthesis procedure of BDN

To prepare BDN, compound BD (500 mg, 1.469 mmol) and 4-(dimethylamino) benzaldehyde (219.28 mg, 1.469 mmol) were dissolved in acetonitrile in a round-bottom flask. Pyrrolidine (121 µl, 1.469 mmol) was added to the mixture, which was then refluxed at 82 °C for 2 hours under an inert atmosphere. After the reaction, the solvent was evaporated, and the crude was purified by column chromatography using a 7 : 3 (v/v) hexane/ethyl acetate mixture. The product was obtained as a greenish-brown solid (450 mg, ~65% yield). R_f (0.30) in 20% ethyl acetate in a hexane solvent mixture. ^1H NMR (400 MHz, DMSO-d_6) δ 9.85 (s, 1H), 7.54–7.33 (m, 3H), 7.23 (d, J = 16.2 Hz, 1H), 7.17–7.06 (m, 2H), 6.96–6.84 (m, 3H), 6.77 (d, J = 8.7 Hz, 2H), 6.11 (s, 1H), 2.99 (s, 6H), 2.45 (s, 3H), 1.47 (s, 3H), 1.41 (s, 3H), (Fig. S1, ESI†) ^{13}C NMR (101 MHz, DMSO) δ 170.8, 158.5, 154.6, 151.6, 145.4, 143.2, 140.6, 138.9, 133.2, 129.8, 129.4, 125.0, 120.8, 116.4, 112.6, 60.2, 31.6, 29.5, 21.2, 15.0, 14.6. (Fig. S2, ESI†) ESI: calculated

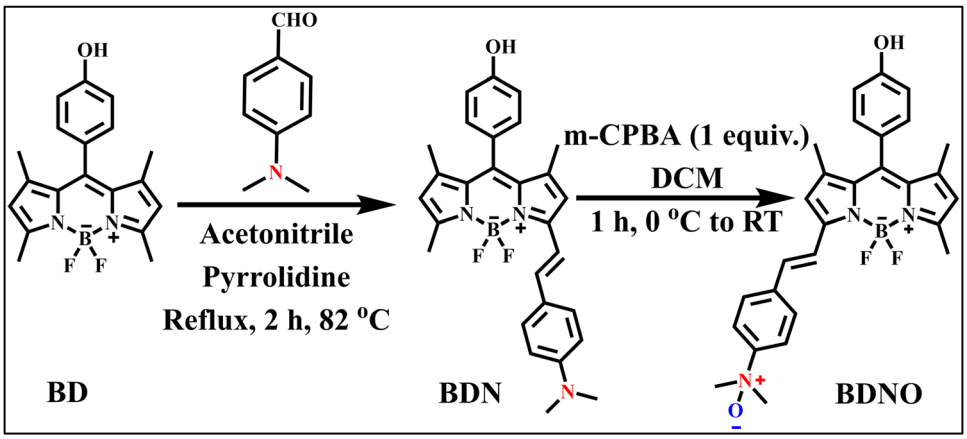

Scheme 2 Structures and the synthetic scheme for synthesizing BDNO.

mass $[M + H]^+$: 472.22, experimental mass $[M + H]^+$: 472.48 (Fig. S3, ESI†).

2.5. Synthesis procedure of BDNO

200 mg, (0.424 mmol) of BDN was dissolved in dichloromethane (DCM) and poured into a round-bottom flask. To this solution, 1 equivalent of *meta*-chloroperoxybenzoic acid (*m*-CPBA, 73 mg, 0.425 mmol) was added incrementally while maintaining the temperature of the solution at 0 °C using an ice bath. After the addition was complete, the reaction mixture was gradually brought to ambient temperature and stirred for another 1 hour. The reaction's progress was monitored through thin-layer chromatography (TLC) until the complete disappearance of the starting material was confirmed. Subsequently, the DCM was removed under vacuum using a rotary evaporator. The resulting residue was washed extensively with DCM and the crude product was purified by column chromatography. R_f = 0.34 (in 10% methanol in DCM solvent system). Yield: 172 mg (83%).

^{1}H NMR (400 MHz, CD_3OD) δ 7.90 (d, J = 8.9 Hz, 2H), 7.65 (d, J = 8.8 Hz, 2H), 7.58 (d, J = 16.4 Hz, 1H), 7.29 (d, J = 16.5 Hz, 1H), 7.08–7.01 (m, 2H), 6.92–6.84 (m, 2H), 6.69 (s, 1H), 6.04 (s, 1H), 3.54 (s, 6H), 2.44 (s, 3H), 1.47 (s, 3H), 1.43 (s, 3H). (Fig. S4, ESI†) MS (ESI) m/z for $C_{28}H_{28}BF_2N_3O_2^-$ $[M - H]^+$ = 486.51, calculated = 486.51 (Fig. S5, ESI†).

2.6. Sample preparation and photo-physical studies

A 1 mM stock solution of the probe (BDNO) was prepared in dimethyl sulfoxide (DMSO), while a 1 mM stock solution of Fe^{2+} ions was prepared using deionized water. For spectral measurements, equal volumes of the Fe^{2+} solution and the probe solution (1 : 1 v/v) to DMSO were used. All experimental setups employed a probe (BDNO) concentration of 20 μM. Fluorescence analyses for Fe^{2+} detection were carried out using a Cary Eclipse spectrophotometer (Agilent Technologies). To assess the selectivity of the probe, potential interference from various metal ions, including Na^+, K^+, Cu^{2+}, Ca^{2+}, Mg^{2+}, Zn^{2+}, Co^{2+}, Mn^{2+}, Ni^{2+}, Ag^+, Li^+, Cd^{2+}, Ba^{2+}, Al^{3+}, Cr^{3+}, Pb^{2+} and Fe^{3+} was examined. Each interfering ion was prepared as a 10 mM aqueous solution. Dual fluorescence excitation was employed at 540 nm and 610 nm, and the corresponding emissions were recorded simultaneously at 570 nm and 715 nm.

3. Results and discussion

3.1. Absorbance and fluorescence response of BDNO in the presence of Fe^{2+}

The parent compound, BDN, with a dimethylamino group, shows a strong absorption peak at 610 nm (Fig. 1A, black curve) and a near-infrared (NIR) fluorescence emission at 715 nm when excited at 610 nm (Fig. 1B, black curve), in the DMSO : H_2O = 1 : 1 solvent system. This is attributed to the electron-donating properties of its dimethylamino group. Upon conversion to its N-oxide derivative (BDNO), the electron-donating ability of the dimethylamino group is reduced, resulting in a hypsochromic shift in the absorption spectrum, with the peak shifting to 540 nm (Fig. 1A). The fluorescence emission also shifts to 570 nm when excited at 540 nm (Fig. 1C, red curve). When Fe^{2+} ions are added, the absorption maximum of BDNO shifts from 540 nm back to 610 nm, matching the original spectrum of BDN. Simultaneously, the fluorescence emission at 570 nm (λ_{ex} = 540 nm) decreases significantly, while the NIR emission at 715 nm (λ_{ex} = 570 nm) increases, demonstrating the probe's ratiometric response. This shift in absorption and fluorescence confirms the reduction of BDNO's N-oxide group by Fe^{2+} ions, regenerating the NIR-fluorescent BDN. Additionally, a visible color change from pink to blue occurs in the presence of Fe^{2+} ions, as shown in Fig. 1A. We measured the fluorescence response of BDNO in the presence and absence of Fe^{2+} using various DMSO : H_2O solvent ratios (5 : 5, 4 : 6, 3 : 7, 2 : 8, 1 : 9, and 0.01 : 99.9), as shown in Fig. S6 (ESI†). BDNO is water-soluble, and the fluorescence emission at 570 nm decreases significantly upon the addition of Fe^{2+}. This quenching is clearly observable even in a DMSO : H_2O ratio of 1 : 9, and even remains detectable in pure water (>99%). However, the fluorescence enhancement at 715 nm (due to the formation of BDN after reduction of BDNO by Fe^{2+}) is prominent only in up to 40% of DMSO in water. As the water content increases

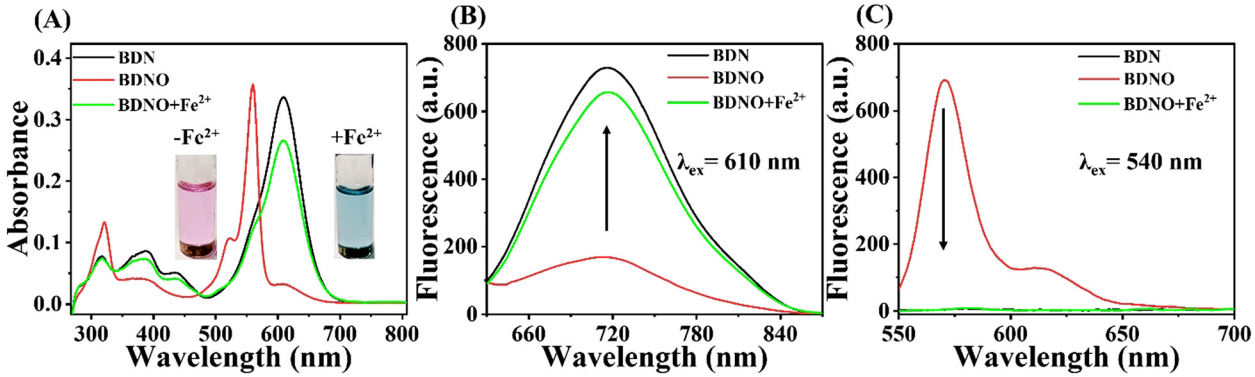

Fig. 1 (A) Absorbance spectra of BDN and BDNO (20 μM in DMSO) with and without Fe^{2+} ions. Emission spectra for BDN and BDNO with and without Fe^{2+} in DMSO at (B) 610 nm excitation and (C) 540 nm excitation. [20 μM of dye (in DMSO) and 20 μM of Fe^{2+} (in water) were used].

beyond this ratio, the emission at 715 nm becomes unmeasurable. We suspect that this is due to the poor solubility of the product (BDN) in high-water-content mixtures. Therefore, when monitoring only the fluorescence emission at 570 nm, it is possible to reduce the DMSO content to as low as 10%.

We further examined the response of the probe BDNO to varying concentrations of Fe^{2+} using UV-Vis and fluorescence spectroscopy. Upon adding Fe^{2+} (0–35 μM) to a 20 μM solution of BDNO, the maximum absorbance peak of the probe gradually shifted from 540 nm to 610 nm (Fig. 2A). A plot of absorbance at 540 nm and 610 nm *versus* Fe^{2+} concentration revealed excellent linearity up to 10 μM, with the signal reaching a plateau upon further addition of Fe^{2+}, as depicted in Fig. 2B. Similarly, the fluorescence emission of BDNO at 570 nm decreased progressively with increasing Fe^{2+} concentration (Fig. 2C). In contrast, the emission at 715 nm increased correspondingly, demonstrating its ratiometric response (Fig. 2D). As shown in Fig. 2E, the fluorescence emissions changes (570 nm and 715 nm) plateaued after the addition of 20 μM Fe^{2+}. The limit of detection (LOD) for Fe^{2+}, determined using the standard formula (LOD = $3\sigma/k$), was

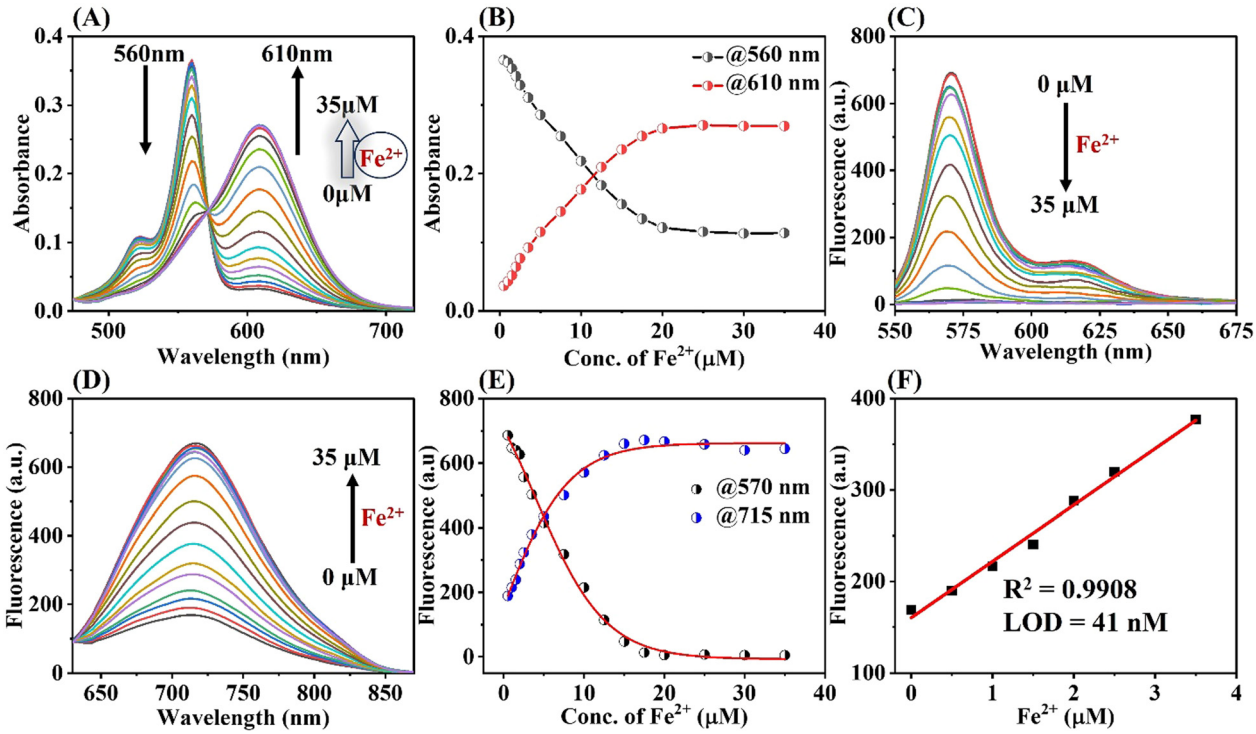

Fig. 2 (A) Absorption spectra of the BDNO probe (20 μM) after the addition of different concentrations (0 to 35 μM) of Fe^{2+} ion. (B) Changes of absorbance at 560 nm and 610 nm with the addition of various concentrations of Fe^{2+} ion. Fluorescence emission at (C) 540 nm excitation and (D) 610 nm excitation in the presence of different concentrations of Fe^{2+} ion in the DMSO–water solvent system. (E) Fluorescence emission changes at 570 nm (when excited at 540 nm) and 715 nm (when excited at 610 nm) with varying concentrations of Fe^{2+}. (F) The linear graph of fluorescence intensity increase vs concentration of Fe^{2+} was used to calculate the limit of detection (LoD), LOD: 41 nM (3σ/slope).

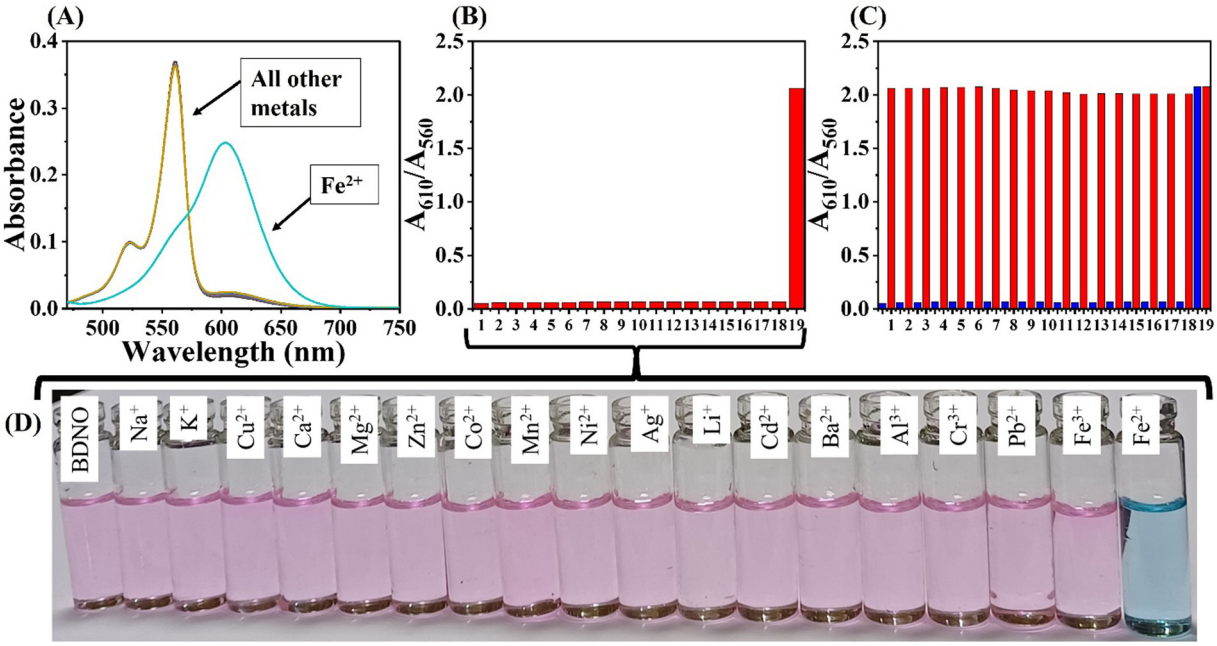

Fig. 3 (A) Absorbance spectra for BDNO (20 μM) against various cations (80 μM) [(1) Probe BDNO, (2) Na^+, (3) K^+, (4) Cu^{2+}, (5) Ca^{2+}, (6) Mg^{2+}, (7) Zn^{2+}, (8) Co^{2+}, (9) Mn^{2+}, (10) Ni^{2+}, (11) Ag^+, (12) Li^+, (13) Cd^{2+}, (14) Ba^{2+}, (15) Al^{3+}, (16) Cr^{3+}, (17) Pb^{2+}, (18) Fe^{3+}, (19) Fe^{2+}]. (B) Ratiometric representation of absorbance at 610 nm and 560 nm (A_{610}/A_{560}) of BDNO in the presence of all the different cations including Fe^{2+}. (C) Absorbance ratio at 610 nm and 560 nm (A_{610}/A_{560}) of BDNO with various different cations (blue bar) and with various cations in the presence of Fe^{2+} ions (red bar). (D) Images of vials containing BDNO (20 μM) with different cations (20 μM) under visible light.

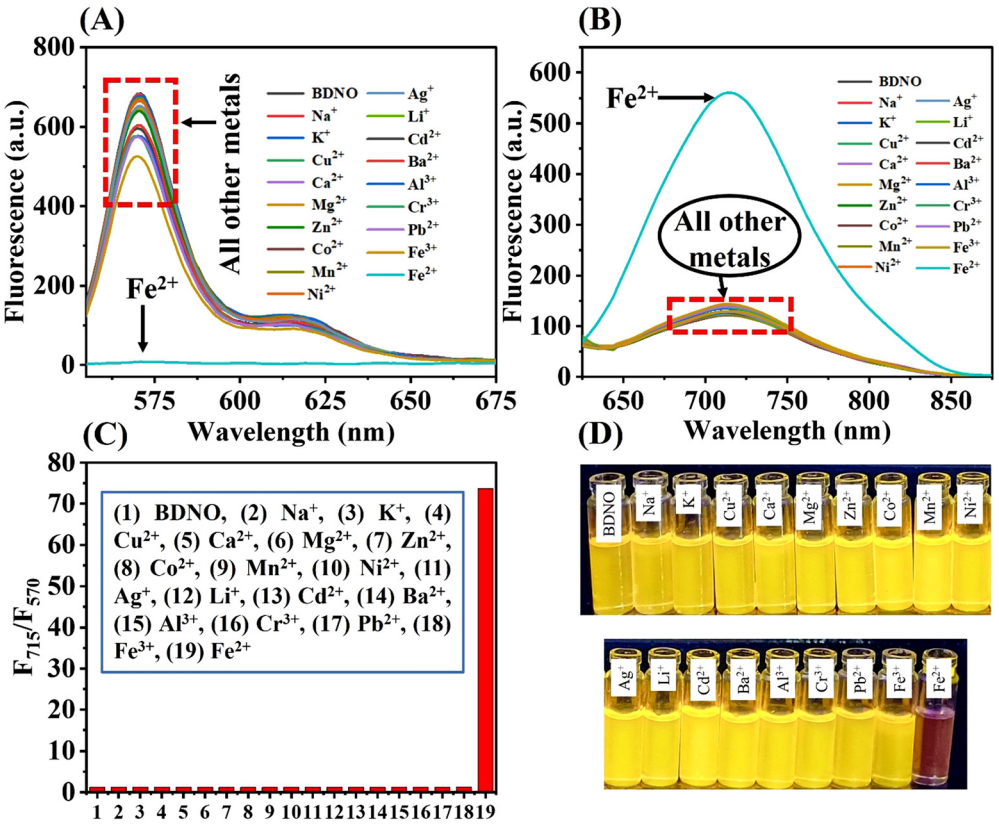

Fig. 4 Fluorescence emission spectra for BDNO (20 μM in DMSO) against various cations (80 μM) at (A) 540 nm excitation and (B) 610 nm excitation. (C) Fluorescence emission ratio (F_{715}/F_{570}) in the presence of various cations. (D) Photo of vials containing BDNO (20 μM) with various cation under UV light [(1) BDNO, (2) Na^+, (3) K^+, (4) Cu^{2+}, (5) Ca^{2+}, (6) Mg^{2+}, (7) Zn^{2+}, (8) Co^{2+}, (9) Mn^{2+}, (10) Ni^{2+}, (11) Ag^+, (12) Li^+, (13) Cd^{2+}, (14) Ba^{2+}, (15) Al^{3+}, (16) Cr^{3+}, (17) Pb^{2+}, (18) Fe^{3+}, (19) Fe^{2+}].

determined to be 41 nM, indicating that BDNO is highly sensitive for Fe^{2+} detection.

3.2. Sensing selectivity of BDNO

The selectivity of the BDNO probe was assessed using UV-Vis absorption spectroscopy in the presence of various potentially interfering cations. As shown in Fig. 3A, the absorption spectrum of the probe remained unchanged in the presence of cations such as Na^+, K^+, Cu^{2+}, Ca^{2+}, Mg^{2+}, Zn^{2+}, Co^{2+}, Mn^{2+}, Ni^{2+}, Ag^+, Li^+, Cd^{2+}, Ba^{2+}, Al^{3+}, Cr^{3+}, Pb^{2+}, and Fe^{3+}, and was similar to that of the probe alone. However, when Fe^{2+} ions were introduced, the probe showed a significant redshift in its absorption maximum from 560 nm to 610 nm (Fig. 3A). The absorbance ratio (A_{610}/A_{560}) clearly indicates the probe's high selectivity toward Fe^{2+} ions, as illustrated in Fig. 3B. Moreover, the presence of the interfering cations did not influence the probe's selectivity for Fe^{2+} (Fig. 3C). The solution exhibited no color change with any interfering cations, and it remained pink, similar to the probe alone. In contrast, the addition of Fe^{2+} caused a noticeable color change from pink to blue (Fig. 3D).

The selectivity of the BDNO probe toward Fe^{2+} ions was further evaluated using fluorescence spectroscopy. As shown in Fig. 4A and B, the probe displayed strong fluorescence emission at 570 nm (λ_{ex} = 540 nm) and weak emission at 715 nm (λ_{ex} = 610 nm) under normal conditions. In the presence of various interfering cations, the fluorescence intensity at both 570 nm and 715 nm remained unchanged. However, upon the addition of Fe^{2+} ions, the fluorescence intensity at 570 nm decreased significantly by approximately 120-fold, while the emission at 715 nm increased substantially (Fig. S7, ESI†). The fluorescence intensity ratio (F_{715}/F_{570}) clearly demonstrated the probe's high selectivity toward Fe^{2+}, with negligible interference from other cations (Fig. 4C). This indicates that the probe functions as a ratiometric sensor for the selective detection of Fe^{2+} ions. Additionally, a noticeable fluorescence color change from yellow to red could be observed with the naked eye under 365 nm UV light in the presence of Fe^{2+} ions (Fig. 4D).

We evaluated the performance of our probe BDNO for Fe^{2+} detection in the presence of various oxidizing and reducing agents, including KI, H_2O_2, and glutathione (GSH). We observed that the fluorescence intensity of the probe (20 μM) remained unchanged upon the addition of these oxidizing and reducing agents (1 mM). Even at a higher concentration of reducing agent GSH (5 mM), no significant change in fluorescence emission was detected, as shown in Fig. S8 (ESI†). These results indicate that the probe is stable in the presence of these oxidizing and reducing agents. Moreover, the presence of these agents does not affect the probe's ability to detect Fe^{2+} ions. Upon the addition of Fe^{2+} in the presence of the oxidizing and reducing agents, we observed a decrease in fluorescence emission at 570 nm and an increase at 715 nm, confirming that these agents do not interfere with Fe^{2+} detection.

3.3. Sensitivity of the probe

The reaction kinetics of the BDNO probe with Fe^{2+} were evaluated by monitoring the fluorescence intensity at 570 nm (λ_{ex} = 540 nm) over time. As shown in Fig. 5A, the fluorescence intensity of the probe BDNO (20 μM) at 570 nm remained stable in the absence of Fe^{2+}. However, upon the addition of Fe^{2+} ions (20 μM), the fluorescence intensity at 570 nm was rapidly quenched, completing the reaction within 5 seconds. This indicates that the probe exhibits an exceptionally fast response to Fe^{2+} ions. To further confirm this rapid reactivity, 20 μM Fe^{2+} was added to a 20 μM solution of the probe, and images were captured over a short time frame under both UV light and visible light. Time-lapse photography showed that the reaction was complete within 5 seconds, with a distinct color change visible to the naked eye under UV light (Fig. 5B) and normal visible light (Fig. 5C). This demonstrates the probe's ability to detect Fe^{2+} ions quickly and with high sensitivity.

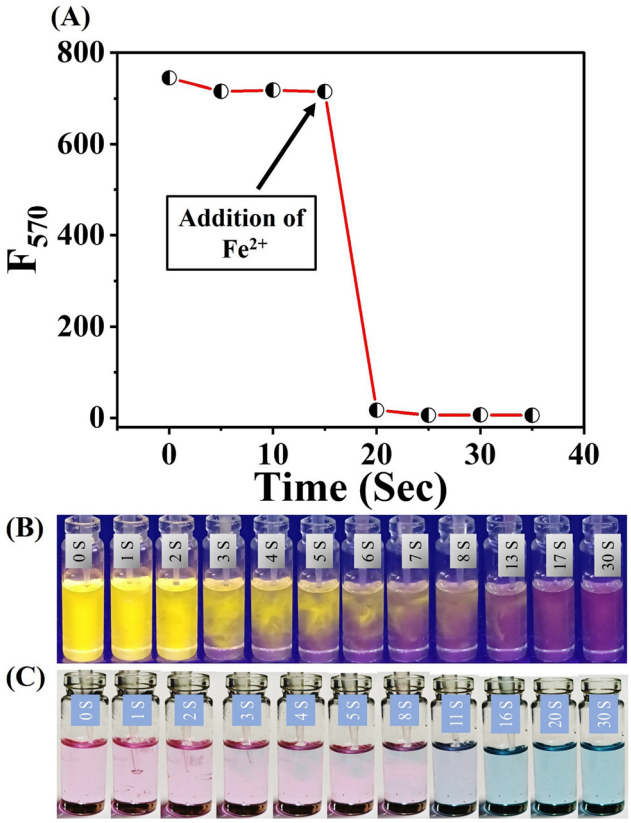

Fig. 5 (A) Time-dependent fluorescence intensity changes at 570 nm (λ_{ex} = 540 nm) of the BDNO probe after the addition of Fe^{2+} (20 μM). Time frame photographs of the vial containing 20 μM in DMSO after the addition of ferrous sulfate (20 μM) in water, (B) under UV light and (C) visible light.

3.4. pH and solvent polarity study

To test whether BDNO works in physiological conditions, we measured its fluorescence stability across different pH levels by recording the fluorescence emission at 570 nm (λ_{ex} = 540 nm) and 715 nm (λ_{ex} = 610 nm) in the presence and absence of Fe^{2+}, as depicted in Fig. S9A and B (ESI†). In the absence of Fe^{2+}, the fluorescence ratio (F_{715}/F_{570}) remained low (Fig. 6, black curve). However, when Fe^{2+} was added, the F_{715}/F_{570} ratio gradually increased with increasing pH, reaching its highest value at pH 7

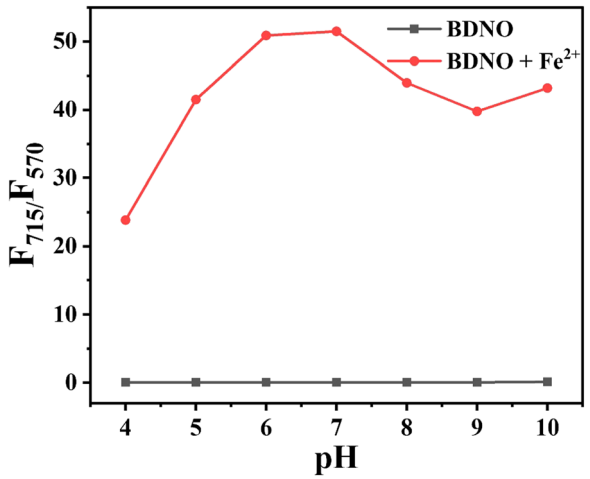

Fig. 6 The fluorescence emission ratio (F_{715}/F_{570}) of the BDNO probe (20 μM) was measured across pH 4–10 in DMSO/water (1 : 1), both in the presence and absence of Fe^{2+} (20 μM).

(Fig. 6, red curve). These results indicate that BDNO is suitable for detecting Fe^{2+} in the pH range from 4 to 10. We also investigated the effect of solvent polarity on Fe^{2+} detection by recording the fluorescence emission of BDNO with and without Fe^{2+} in three different solvents—DMF, DMSO, and methanol (Fig. S10 and S11, ESI†). In all cases, the presence of Fe^{2+} led to a decrease in emission at 570 nm and an increase at 715 nm. Notably, as the solvent polarity decreased from DMSO to methanol, the emission peaks exhibited slight blue shifts, with emissions at 570 and 715 nm shifting to 567 and 674 nm, respectively.

3.5. Detection of Fe^{2+} by paper strip, cotton bud and bean sprouts

The practical applicability of the BDNO probe was evaluated by detecting Fe^{2+} using filter paper as a portable detection platform. For this study, Whatman grade-1 filter paper was used. A 100 μM solution of BDNO in methanol was prepared, and the

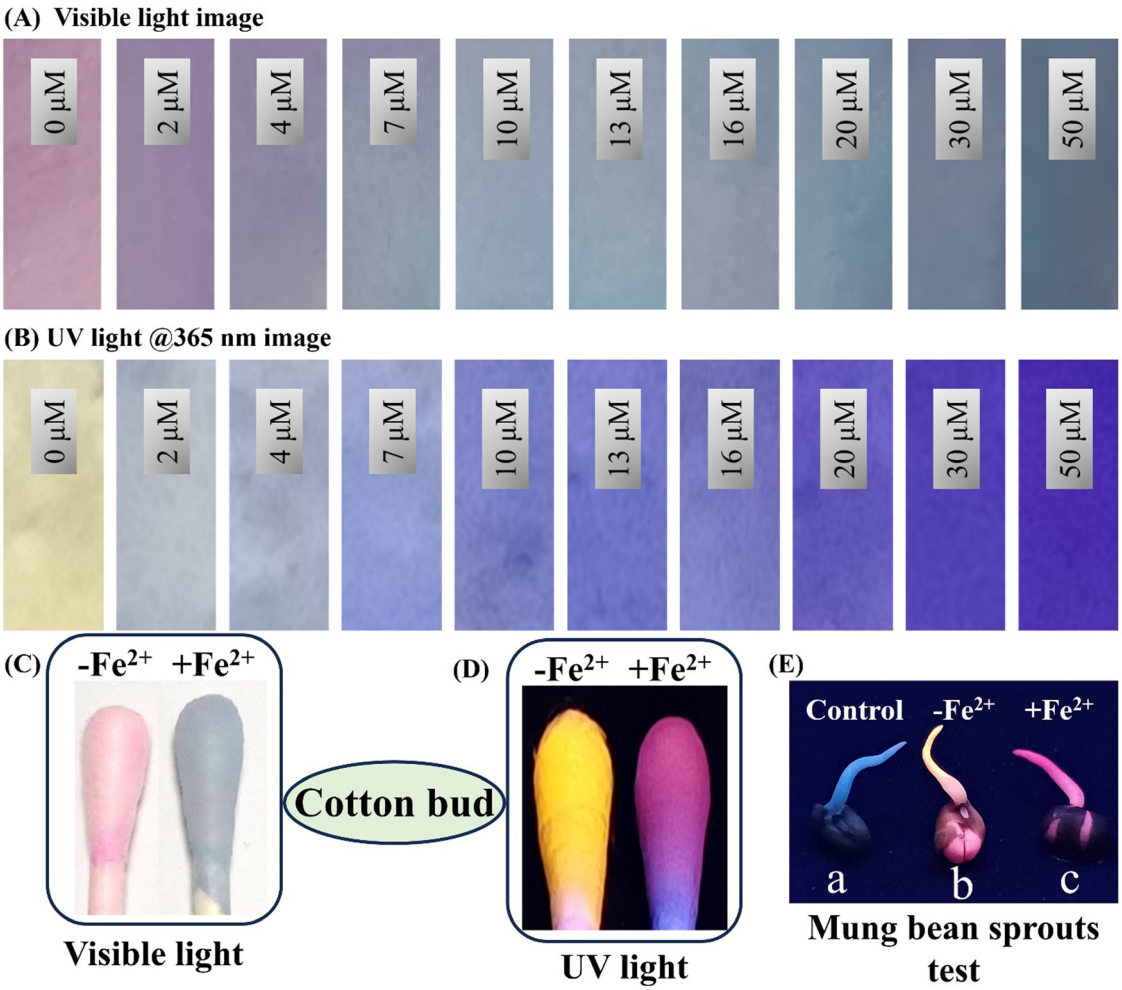

Fig. 7 Detection of Fe^{2+} using a paper strip and cotton bud. (A) and (B) The probe BDNO (100 μM) was absorbed onto filter paper, dried, and treated with varying concentrations of Fe^{2+} (0 to 50 μM). Photographs were captured under (A) visible and (B) UV light. (C) and (D) Detection of Fe^{2+} using a cotton bud: the probe was absorbed into the cotton bud, and Fe^{2+} (20 μM) was subsequently added. Images were taken under (C) visible light and (D) UV light. (E) Fluorescent images of mung bean sprouts under UV illumination: (a) control (untreated bean), (b) bean treated with the BDNO probe, and (c) bean treated with the BDNO probe in the presence of Fe^{2+} ions.

filter paper was soaked in the solution for two minutes and then air-dried. The prepared strips were subsequently exposed to aqueous solutions containing varying concentrations of Fe^{2+} (0, 2, 4, 7, 10, 13, 16, 20, 30, and 50 μM) and air-dried. Distinct color changes were visible on the strips with the naked eye as the Fe^{2+} concentration increased. Under visible light, the color changed from red to blue (Fig. 7A and Fig. S12A, ESI†), while under a handheld UV lamp, the color shifted from yellow to reddish-blue (Fig. 7B and Fig. S12B, ESI†). In contrast, no noticeable color changes were observed when the strips were exposed to other cations, such as Na^{+}, K^{+}, Cu^{2+}, Ca^{2+}, Mg^{2+}, Zn^{2+}, Co^{2+}, Mn^{2+}, Ni^{2+}, Ag^{+}, Li^{+}, Cd^{2+}, Ba^{2+}, Al^{3+}, Cr^{3+}, Pb^{2+}, and Fe^{3+}, as shown in Fig. S13 (ESI†). It is particularly advantageous for field testing, where access to traditional laboratory instruments may be limited. Additionally, the distinct visual color changes enhance the method's effectiveness for real-world applications.

We evaluated Fe^{2+} detection using mung bean sprouts. As a control experiment, sprouts were first imaged under UV light without any probe, showing no fluorescence (Fig. 7E(a)). In the next step, the sprouts were soaked in a 100 μM solution of BDNO for 10 min, followed by thorough rinsing with distilled water. Upon UV illumination, the sprouts exhibited a distinct yellow fluorescence (Fig. 7E(b)). Subsequently, the BDNO-treated sprouts were immersed in a 50 μM Fe^{2+} solution for 30 s, washed again, and imaged under UV light. Notably, the

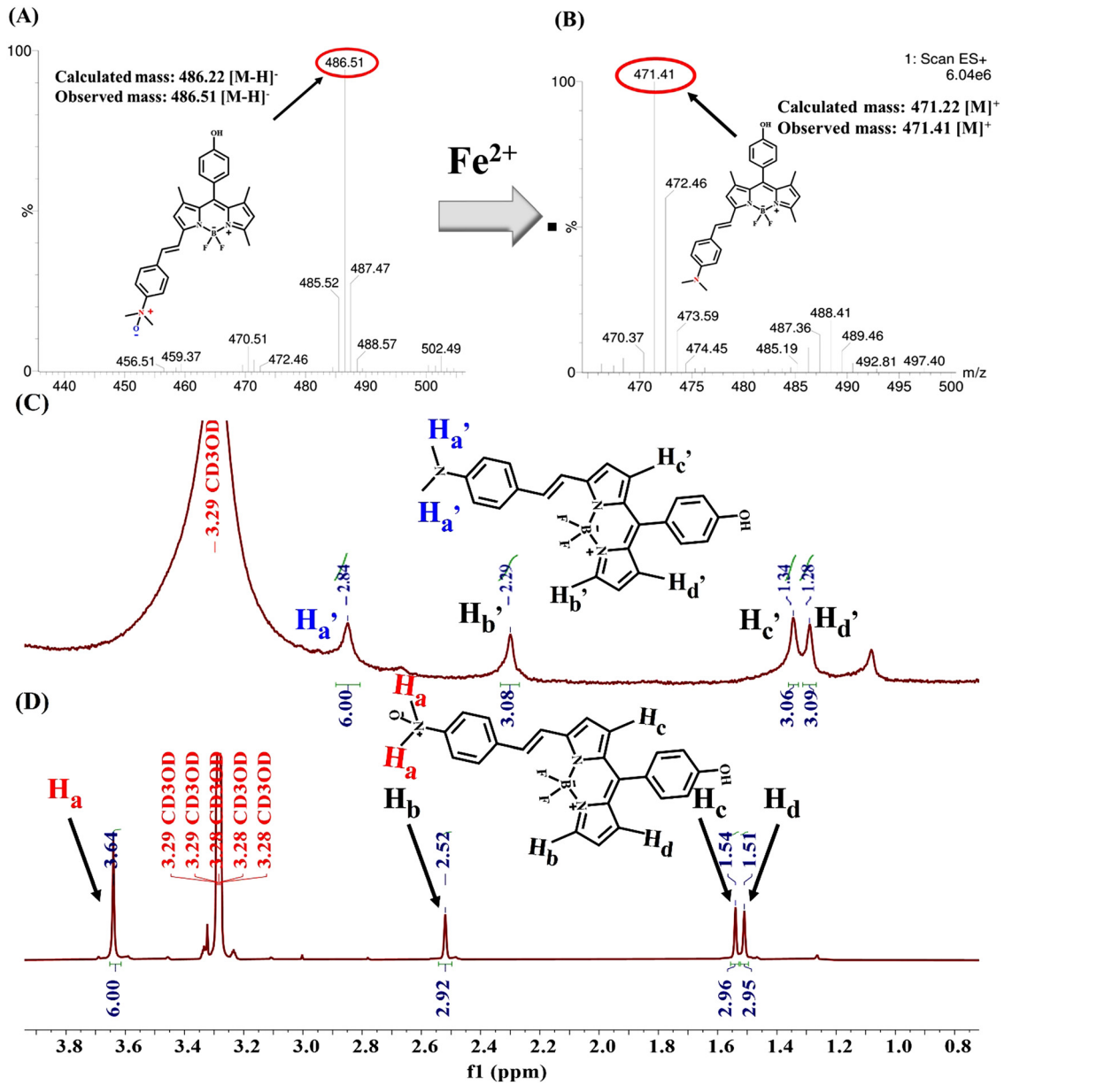

Fig. 8 Proposed mechanism of Fe^{2+} detection by mass spectrometry. Mass spectrum of the probe (A) without Fe^{2+} and (B) with Fe^{2+} ions. Partial ^{1}H NMR spectra of the BDNO in the (C) presence and (D) absence of Fe^{2+} in CD_3OD.

fluorescence shifted from yellow to pink (Fig. 7E(c)), clearly indicating the successful detection of Fe^{2+}. These results demonstrate the potential of BDNO for Fe^{2+} sensing in plant systems.

3.6. Mechanistic investigation of BDNO to detect Fe^{2+}

To explore the mechanism behind BDNO's detection of Fe^{2+}, 10 equivalents of Fe^{2+} were added to the BDNO probe in methanol, and the resulting solution was analyzed using mass spectrometry. The BDNO probe without Fe^{2+} was used as a control. The ESI-MS analysis revealed a molecular peak at m/z 486.51, corresponding to the BDNO probe for the control sample (Fig. 8A). However, in the presence of Fe^{2+} ions, a new peak appeared at m/z 471.41, which corresponds to the BDN molecule (Fig. 8B and Fig. S14, ESI†). This result provides clear evidence supporting our proposed reduction mechanism, where the N-oxide state (BDNO) is reduced to the amine state (BDN) in the presence of Fe^{2+}.

To confirm the reduction, we carried out a simple TLC experiment. First, we spotted only the BDNO probe on the TLC plate (Fig. S15, spot a, ESI†). Next to it, we spotted a mixture of BDNO and Fe^{2+} (spot b). As a positive control, we also spotted the reduced form, BDN (spot c). The TLC was run using a solvent mixture of 20% ethyl acetate in hexane. After running the TLC, we checked it under visible light, 254 nm, and 363 nm UV light, as shown in Fig. S15 (ESI†). We found that the BDNO with Fe^{2+} spot (spot b) had almost the same R_f value as the BDN spot (spot c). This indicates that BDNO is reduced by Fe^{2+} to form the same product as BDN. To gain deeper insight into the reaction mechanism of BDNO in the presence of Fe^{2+}, we examined the ^{1}H NMR spectra of BDNO in CD_3OD, both with and without Fe^{2+} (Fig. 8C and D). In the absence of Fe^{2+}, the *N*,*N*′-dimethyl protons (H_a) appeared at 3.64 ppm (Fig. 8D). However, upon the addition of Fe^{2+} (10 equivalents), this signal shifted upfield to 2.84 ppm, as shown in Fig. 8C. It is well established that oxidation of the *N*,*N*′-dimethyl group to form an N-oxide induces a downfield shift in adjacent methyl protons. Therefore, the observed upfield shift strongly supports the reduction of the N-oxide moiety by Fe^{2+}. The interaction between BDNO and Fe^{2+} was further validated by FT-IR spectroscopy (Fig. S16, ESI†). BDNO exhibited a characteristic N–O stretching vibration at 1381 cm^{-1}, indicating the presence of the N-oxide group. Upon treatment with Fe^{2+}, this characteristic band disappeared, indicating the cleavage of the N–O bond. These FT-IR results provide additional evidence that Fe^{2+} reduces the N-oxide moiety in BDNO.

3.7. Detection of Fe^{2+} in food and water samples

Next, we tested the probe's ability to detect Fe^{2+} in real samples, including tap water, river water, sea water, wine, apple juice, and orange juice. First, we added 20 μM of the BDNO probe to each sample, and the fluorescence emission at 570 nm was recorded. The concentration of Fe^{2+} was then determined using a standard concentration curve. In a separate test, we added different amounts of Fe^{2+} to the samples and calculated the concentrations of Fe^{2+} again using the same method. The results, as shown in Table 1, are the average of 3 separate experiments and show excellent recovery rates (above 80% recovery). These findings confirm that the BDNO probe is sensitive and can detect very small amounts of Fe^{2+} in real samples. Its performance across various samples makes it a reliable tool for detecting Fe^{2+}, with potential applications in food safety and water quality.

Table 1 Analysis of Fe^{2+} in real samples, tap water, river water and sea water

	Added Fe^{2+} (μM)	Found ± standard deviation (μM) (calibration curve method)	Recovery ± standard deviation (%)
Apple juice	0	0.63 ± 0.16	—
	3	3.33 ± 0.10	91.73 ± 0.89
	10	10.24 ± 0.34	96.33 ± 0.57
Orange juice	0	0.38 ± 0.25	—
	3	3.25 ± 0.19	96.15 ± 0.38
	10	10.12 ± 0.24	97.49 ± 0.16
Wine	0	0.25 ± 0.03	—
	3	2.98 ± 0.36	91.69 ± 0.54
	10	10.05 ± 0.62	98.04 ± 0.26
Tap water	3	2.96 ± 0.13	98.98 ± 0.54
	5	4.84 ± 0.44	96.93 ± 0.29
	7	6.80 ± 0.49	97.20 ± 0.48
	9	8.57 ± 0.56	95.26 ± 0.26
River water	0	0.05 ± 0.01	—
	3	2.52 ± 0.02	82.33 ± 0.50
	10	8.83 ± 0.04	88.0 ± 0.43
Sea water	0	0.03 ± 0.04	—
	3	2.45 ± 0.02	81.67 ± 0.67
	10	8.67 ± 0.05	86.2 ± 0.58

Table 2 Smartphone-based colorimetric paper strip method for detecting Fe^{2+} in water samples

Spiked Fe^{2+} (μM)	Test paper	Test paper-smartphone (μM)	Recovery (%) of test paper-smartphone probe
4		3.66	91.5
7		6.74	96.28
10		9.34	93.4

3.8. Smartphone-based quantitative detection of Fe^{2+} using paper strips

Using the paper strip images from Fig. 6A and B, the digital information (RGB value) of these images was obtained by color recognition software installed on a smartphone. A good linear correlation was observed between Fe^{2+} concentration and B/R value (Fig. S17, ESI†). To validate the practicality of the smartphone-assisted test strip detection platform for on-site and field detection of Fe^{2+} in water samples, we conducted the detection of spiked Fe^{2+} content in tap water samples, using a smartphone. Various sample solutions with spiked Fe^{2+} were prepared in 4, 7, and 10 μM concentrations. The sample solution was then dropped onto the test strip, which was previously dipped with BDNO and air-dried. Because of the Fe^{2+} in the sample solution, the fluorescence color of the test strip changed, and the RGB value of these paper strips was calculated using a smartphone, and the Fe^{2+} concentration was calculated from the calibration curve (Fig. S17, ESI†). The detection results are shown in Table 2, which indicates a satisfactory recovery rate of 91.5–96.28%.

4. Conclusions

In conclusion, we have developed a ratiometric near-infrared (NIR) fluorescent probe, BDNO, for the selective detection of Fe^{2+} ions. The probe exhibits a dual fluorescence response, with fluorescence quenching at 570 nm (λ_{ex} = 540 nm) and enhancement at 715 nm (λ_{ex} = 610 nm), accompanied by distinct and visually observable color changes from pink to blue in the presence of Fe^{2+} ions. BDNO demonstrates outstanding selectivity, sensitivity and specificity for Fe^{2+}, with minimal interference from other biologically relevant cations. Its rapid response time (<5 s), nanomolar-level detection limits (LoD 41 nM), and ability to accurately detect Fe^{2+} in various food samples (*e.g.*, apple juice, orange juice, wine, tap, river, and seawater) highlight its potential for food safety monitoring. The probe's usefulness for field-based and point-of-care diagnostics is further demonstrated by its capacity to detect Fe^{2+} ions on paper strips and cotton buds with the naked eye without the need for sophisticated equipment.

Author contributions

Aindam Mondal: probe syntheses, formal analysis, data collection, original draft writing; Sudip Mondal: formal analysis, data collection; Adinath Majee: formal analysis, writing – review & editing, Subrata Dutta: supervision, formal analysis, writing – review & editing, project administration.

Data availability

All data are available in the ESI.†

Conflicts of interest

The authors declare no competing financial interests.

Acknowledgements

Subrata Dutta acknowledges the Science and Engineering Research Board (SERB), New Delhi, for a Start-up Research grant (SRG) (SRG/2021/001215) and SVNIT, Surat for the Seed Grant (Project No. 2021-22/DoC/19) for financial support.

References

1 P. A. Frey and G. H. Reed, *ACS Chem. Biol.*, 2012, **7**, 1477–1481.
2 A. S. Fleischhacker and P. J. Kiley, *Curr. Opin. Chem. Biol.*, 2011, **15**, 335–341.
3 L. Ma, M. Gholam Azad, M. Dharmasivam, V. Richardson, R. J. Quinn, Y. Feng, D. L. Pountney, K. F. Tonissen, G. D. Mellick, I. Yanatori and D. R. Richardson, *Redox Biol.*, 2021, **41**, 101896.
4 O. Kakhlon and Z. I. Cabantchik, *Free Radical Biol. Med.*, 2002, **33**, 1037–1046.
5 R. C. Hider and X. L. Kong, *Biometals*, 2011, **24**, 1179–1187.
6 R. Hider, M. V. Aviles, Y.-L. Chen and G. O. Latunde-Dada, *Int. J. Mol. Sci.*, 2021, **22**, 1278.
7 S. Oshiro, M. S. Morioka and M. Kikuchi, *Adv. Pharmacol. Pharm. Sci.*, 2011, 378278.
8 S. Recalcati, E. Gammella and G. Cairo, *Free Radicals Biol. Med.*, 2019, **133**, 216–220.
9 S. Toyokuni, *Cancer Sci.*, 2009, **100**, 9–16.
10 E. Madsen and J. D. Gitlin, *Annu. Rev. Neurosci.*, 2007, **30**, 317–337.
11 L. Zecca, M. B. H. Youdim, P. Riederer, J. R. Connor and R. R. Crichton, *Nat. Rev. Neurosci.*, 2004, **5**, 863–873.
12 Y. Xie, W. Hou, X. Song, Y. Yu, J. Huang, X. Sun, R. Kang and D. Tang, *Cell Death Differ.*, 2016, **23**, 369–379.
13 S. J. Dixon, K. M. Lemberg, M. R. Lamprecht, R. Skouta, E. M. Zaitsev, C. E. Gleason, D. N. Patel, A. J. Bauer, A. M. Cantley, W. S. Yang, B. Morrison, III and B. R. Stockwell, *Cell*, 2012, **149**, 1060–1072.
14 S. Carter, A. S. Fisher, M. W. Hinds, S. Lancaster and J. Marshall, *J. Anal. At. Spectrom.*, 2013, **28**, 1814–1869.

15 M. West, A. T. Ellis, P. J. Potts, C. Streli, C. Vanhoof and P. Wobrauschek, *J. Anal. At. Spectrom.*, 2016, **31**, 1706–1755.
16 Z.-Q. Liang, C.-X. Wang, J.-X. Yang, H.-W. Gao, Y.-P. Tian, X.-T. Tao and M.-H. Jiang, *New J. Chem.*, 2007, **31**, 906–910.
17 S.-H. Chen, Y.-X. Li, P.-H. Li, X.-Y. Xiao, M. Jiang, S.-S. Li, W.-Y. Zhou, M. Yang, X.-J. Huang and W.-Q. Liu, *TrAC, Trends Anal. Chem.*, 2018, **106**, 139–150.
18 L. M. Laglera and D. Monticelli, *Curr. Opin. Electrochem.*, 2017, **3**, 123–129.
19 Y.-Y. Zhang, X.-Z. Chen, X.-Y. Liu, M. Wang, J.-J. Liu, G. Gao, X.-Y. Zhang, R.-Z. Sun, S.-C. Hou and H.-M. Wang, *Sens. Actuators, B*, 2018, **273**, 1077–1084.
20 Y. W. Choi, G. J. Park, Y. J. Na, H. Y. Jo, S. A. Lee, G. R. You and C. Kim, *Sens. Actuators, B*, 2014, **194**, 343–352.
21 A. T. Aron, M. O. Loehr, J. Bogena and C. J. Chang, *J. Am. Chem. Soc.*, 2016, **138**, 14338–14346.
22 H. Y. Au-Yeung, J. Chan, T. Chantarojsiri and C. J. Chang, *J. Am. Chem. Soc.*, 2013, **135**, 15165–15173.
23 Z. I. Cabantchik, H. Glickstein, P. Milgram and W. Breuer, *Anal. Biochem.*, 1996, **233**, 221–227.
24 T. Hirayama, *Free Radicals Biol. Med.*, 2019, **133**, 38–45.
25 F. Petrat, H. de Groot and U. Rauen, *Arch. Biochem. Biophys.*, 2000, **376**, 74–81.
26 W. Breuer, S. Epsztejn and Z. I. Cabantchik, *J. Biol. Chem.*, 1995, **270**, 24209–24215.
27 S. Wei, L. Tan, X. Yin, R. Wang, X. Shan, Q. Chen, T. Li, X. Zhang, C. Jiang and G. Sun, *Analyst*, 2020, **145**, 2357–2366.
28 M. Azami, M. Valizadehderakhshan, P. Tukur and J. Wei, *J. Photochem. Photobiol., A*, 2024, **446**, 115111.
29 C.-F. Wan, Y.-J. Chang, C.-Y. Chien, Y.-W. Sie, C.-H. Hu and A.-T. Wu, *J. Lumin.*, 2016, **178**, 115–120.
30 M. Niwa, T. Hirayama, I. Oomoto, D. O. Wang and H. Nagasawa, *ACS Chem. Biol.*, 2018, **13**, 1853–1861.
31 T. Hirayama, K. Okuda and H. Nagasawa, *Chem. Sci.*, 2013, **4**, 1250–1256.
32 T. Mukaide, Y. Hattori, N. Misawa, S. Funahashi, L. Jiang, T. Hirayama, H. Nagasawa and S. Toyokuni, *Free Radical Res.*, 2014, **48**, 990–995.
33 M. Niwa, T. Hirayama, K. Okuda and H. Nagasawa, *Org. Biomol. Chem.*, 2014, **12**, 6590–6597.
34 Z. Liu, S. Wang, W. Li and Y. Tian, *Anal. Chem.*, 2018, **90**, 2816–2825.
35 J. Zheng, S. Feng, S. Gong, Q. Xia and G. Feng, *Sens. Actuators, B*, 2020, **309**, 127796.
36 X. Zhang, Y. Chen, X. Cai, C. Liu, P. Jia, Z. Li, H. Zhu, Y. Yu, K. Wang, X. Li, W. Sheng and B. Zhu, *Dyes Pigm.*, 2020, **174**, 108065.
37 W. Xuan, R. Pan, Y. Wei, Y. Cao, H. Li, F.-S. Liang, K.-J. Liu and W. Wang, *Bioconjugate Chem.*, 2016, **27**, 302–308.
38 Z. Qu, P. Li, X. Zhang and K. Han, *J. Mater. Chem. B*, 2016, **4**, 887–892.
39 T. Hirayama and H. Nagasawa, *J. Clin. Biochem. Nutr.*, 2017, **60**, 39–48.
40 R. Kouser, S. Zehra, R. A. Khan, A. Alsalme, F. Arjmand and S. Tabassum, *Spectrochim. Acta, Part A*, 2021, **247**, 119156.
41 S. Lee, A. Uliana, M. K. Taylor, K. Chakarawet, S. R. S. Bandaru, S. Gul, J. Xu, C. M. Ackerman, R. Chatterjee, H. Furukawa, J. A. Reimer, J. Yano, A. Gadgil, G. J. Long, F. Grandjean, J. R. Long and C. J. Chang, *Chem. Sci.*, 2019, **10**, 6651–6660.
42 L. Long, N. Wang, Y. Han, M. Huang, X. Yuan, S. Cao, A. Gong and K. Wang, *Analyst*, 2018, **143**, 2555–2562.
43 S. Santhoshkumar, K. Velmurugan, J. Prabhu, G. Radhakrishnan and R. Nandhakumar, *Inorg. Chim. Acta*, 2016, **439**, 1–7.
44 S. D. Padghan, A. L. Puyad, R. S. Bhosale, S. V. Bhosale and S. V. Bhosale, *Photochem. Photobiol. Sci.*, 2017, **16**, 1591–1595.
45 P. Feng, L. Ma, F. Xu, X. Gou, L. Du, B. Ke and M. Li, *Talanta*, 2019, **203**, 29–33.
46 X. Yang, Y. Wang, R. Liu, Y. Zhang, J. Tang, E.-B. Yang, D. Zhang, Y. Zhao and Y. Ye, *Sens. Actuators, B*, 2019, **288**, 217–224.
47 J.-L. Chen, S.-J. Zhuo, Y.-Q. Wu, F. Fang, L. Li and C.-Q. Zhu, *Spectrochim. Acta, Part A*, 2006, **63**, 438–443.
48 G.-G. Hou, C.-H. Wang, J.-F. Sun, M.-Z. Yang, D. Lin and H.-J. Li, *Biochem. Biophys. Res. Commun.*, 2013, **439**, 459–463.
49 H. Xiang, Y. Song, Y. Wang, W. Fu and N. Xiao, *Mater. Adv.*, 2024, **5**, 5624–5631.
50 A. Ciupa, *RSC Adv.*, 2024, **14**, 3519–3524.
51 Y. Zhou, X. Yang, W. J. Jang, M. Yan and J. Yoon, *Coord. Chem. Rev.*, 2025, **522**, 216201.
52 T. Hirayama, H. Tsuboi, M. Niwa, A. Miki, S. Kadota, Y. Ikeshita, K. Okuda and H. Nagasawa, *Chem. Sci.*, 2017, **8**, 4858–4866.
53 S. Feng, J. Zheng, J. Zhang, Z. Gui and G. Feng, *Sens. Actuators, B*, 2022, **371**, 132512.
54 Y. Dubey, S. Mansuri and S. Kanvah, *J. Mater. Chem. B*, 2024, **12**, 4962–4974.
55 E. Ahmmed, A. Mondal, A. Sarkar, S. Chakraborty, S. Lohar, N. C. Saha, K. Dhara and P. Chattopadhyay, *ACS Appl. Bio Mater.*, 2020, **3**, 4074–4080.
56 S. Banfi, E. Caruso, S. Zaza, M. Mancini, M. B. Gariboldi and E. Monti, *J. Photochem. Photobiol., B*, 2012, **114**, 52–60.

